

PAPER • OPEN ACCESS

Anodic alumina/carbon composite films: extraction and characterization of the carbon-containing component

To cite this article: Katsiaryna Chernyakova *et al* 2024 *J. Phys. Mater.* **7** 025011

View the [article online](#) for updates and enhancements.

You may also like

- [Small size 2-DOF piezoelectric platform for unlimited locomotion](#)
A eponis, D Mažeika, V Jrnas et al.
- [Calibration of the MACHO Photometric System: \$VR_{off}\$ and \$BC_v\$ Calibration for Metalpoor Giants](#)
Michael S. Bessell and Lisa M. Germany
- [Analysis of measurement system as the mechatronics system](#)
V Giniotis, K T V Grattan, M Rybokas et al.



PRIME
PACIFIC RIM MEETING
ON ELECTROCHEMICAL
AND SOLID STATE SCIENCE

HONOLULU, HI
Oct 6–11, 2024

Abstract submission
deadline extended:
April 19, 2024
Learn more and submit!

Joint Meeting of
The Electrochemical Society
•
The Electrochemical Society of Japan
•
Korea Electrochemical Society



PAPER

OPEN ACCESS

Anodic alumina/carbon composite films: extraction and characterization of the carbon-containing component

RECEIVED
31 October 2023REVISED
27 February 2024ACCEPTED FOR PUBLICATION
5 April 2024PUBLISHED
17 April 2024Katsiaryna Chernyakova^{1,*} , Ieva Matulaitienė¹ , Tatjana Charkova¹ , Giedrė Grincienė¹ ,
Meda Jurevičiūtė² , Aurimas Kopūstas^{1,2} , Arūnas Jagminas¹  and Renata Karpicz¹ ¹ Centre for Physical Sciences and Technology, Sauletekio av. 3, LT-10257 Vilnius, Lithuania² Vilnius University, Life Sciences Center, Institute of Biotechnology, Sauletekio av. 7, LT-10257 Vilnius, Lithuania

* Author to whom any correspondence should be addressed.

E-mail: katsiaryna.charniakova@ftmc.lt**Keywords:** anodic alumina, formic acid, amorphous carbon nanoparticles, fluorescence, biocompatibilityOriginal content from
this work may be used
under the terms of the
[Creative Commons
Attribution 4.0 licence](https://creativecommons.org/licenses/by/4.0/).Any further distribution
of this work must
maintain attribution to
the author(s) and the title
of the work, journal
citation and DOI.**Abstract**

Alumina/carbon composites are modern nanomaterials used as adsorbents, catalysts, catalyst supports, supercapacitors, and electrode materials for fuel cells. Among other methods, aluminum anodizing is fairly fast and inexpensive for producing anodic alumina/carbon composites with controllable properties. In the present study, the morphology and composition of carbon-enriched anodic alumina films were obtained during aluminum anodic oxidation in formic acid with ammonium heptamolybdate (C content is ca. 5.0 mass%) or oxalic acid (C content 3.4 mass%) additives. The anodic alumina films have a wide blue fluorescence (FL) in the 400–650 nm wavelength range with a maximum at ca. 490 nm. The FL decay is nonexponential and has an average lifetime of 1.54 and 1.59 ns for ammonium heptamolybdate and oxalic acid additives, respectively. As samples obtained in sulfuric acid (i.e. without carbon) do not possess detectable FL in the 400–650 nm wavelength range, it was concluded that carbon-containing inclusions are responsible for the FL properties of the films. The initial samples were dissolved in the hot aqueous HCl solution and then dialyzed to extract the carbon-containing component. It was shown that the solutions contain nanoparticles of amorphous carbon with a 20–25 nm diameter. Carbon nanoparticles also exhibit an excitation-dependent emission behavior at 280–450 nm excitation wavelengths with average lifetimes of 7.25–8.04 ns, depending on the composition of the initial film. Carbon nanoparticle FL is caused by the core of carbon nanoparticles (CNPs) and various emission centers on their surface, such as carbonyl, carboxyl, and hydroxyl groups. As CNPs could be exceptional candidates for detection technologies, the biocompatibility assays were performed with living COS-7 mammalian cells, showing a minimal negative impact on the living cells.

1. Introduction

Alumina/carbon composites are modern nanomaterials used as adsorbents, catalysts, catalyst supports, supercapacitors, and electrode materials for fuel cells [1–3]. There are many ways to obtain alumina/carbon composites: solution combustion [4], template [5], carbon precursor [6], simple wet [7], aluminum anodizing in organic acid solutions [8–10], and plasma electrolytic oxidation techniques [11], and the choice of synthesis methods and conditions will determine the properties of the final composites. Among the methods mentioned is aluminum anodizing, a fairly fast, inexpensive method of producing nanostructured alumina with controllable properties by electrochemical oxidation of aluminum and its alloys in solutions of various electrolytes [12]. Moreover, anodizing conditions, such as anodizing voltage, electrolyte nature, concentration, and temperature, significantly affect the properties, morphology, and composition of the samples. Depending on the electrolyte nature, aluminum anodizing forms two types of oxide films, i.e. barrier and porous. Barrier-type films cannot be obtained with a thickness of more than a few micrometers, while the thickness of porous films can reach several hundred micrometers [13, 14]. Therefore,

porous films are more popular in industry and the scientific community. Besides, anodizing conditions are quite easy to regulate and control [14]. In industry, aqueous oxalic, sulfuric, and phosphoric acid solutions are often used for aluminum anodizing. For research purposes, acids such as malonic, glycolic, tartaric, citric, or even squaric acids can also be applied [13–19].

Generally, the following steps are considered during aluminum anodizing: aluminum is oxidized at the Al|Al₂O₃ interface, yielding Al³⁺ ions. These cations drift through the oxide layer due to the electric field and are ejected into the solution at the Al₂O₃|electrolyte interface. At the Al₂O₃|solution interface, oxygen ions from water of OH⁻ ion oxidation enter the oxide. At the same time, oxygen-containing ions, such as O²⁻ and OH⁻, migrate from the electrolyte|Al₂O₃ interface through the oxide layer to the Al|Al₂O₃ interface, resulting in metal oxidation. Electrolyte anions are adsorbed at the pore bottom|electrolyte interface, and depending on the electrolyte type, they can be immobile and migrate inward or outward throughout the oxide under the electric field [14, 18, 20–22]. Electrolyte ions can also undergo electrochemical transformation; for example, oxalates and tartrates can be oxidized [8, 23]. At the same time, sulfates or phosphates do not change their state. Therefore, electrolyte ions or products of their oxidation are incorporated into the porous alumina [12, 13, 24]. The content of electrolyte-derived species depends on anodizing conditions and electrolyte nature and usually varies from 10 to 12 at% for sulfuric acid anodizing and 2–3 at% for oxalic acid anodizing [13, 14, 25–29]. Obviously, these species affect not only the electrochemical process of aluminum oxidation (changing the structure of the double-layer at the Al₂O₃|electrolyte interface) but also the composition and physical–chemical properties of anodic alumina (AA) films (creating impurities and additional defects in the alumina) [30–34]. So, the nature and mechanism of fluorescence (FL) of AA films obtained in various electrolytes have been debated for many years. In the case of sulfuric acid anodizing, oxygen vacancies or other structure defects can be responsible for the FL of AA. However, the situation is not so determined for anodizing in organic acid solutions as carbon-containing inclusions are also optically active [35, 36]. Some authors believe that only oxygen defects determine the electronic and optical properties of anodic alumina [31, 37–39]. Others suggest that the FL could be attributed to organic impurities, such as carboxylate species and amorphous carbon [8, 40–42].

Even though it is commonly accepted that anodic films thicker than 100 nm on the aluminum surface cannot be formed in monocarboxylic acid solutions [43], it was shown that formic acid AA could be formed at relatively high temperatures and concentrations [44–46]. Moreover, using complex electrolytes containing formic acid with additives resulted in the formation of porous irregular oxide layers. According to the existing ideas, when organic compounds and/or complex oxyanions are added to the electrolyte solutions, they can not only reduce the rate of anodic oxidation but also inhibit the chemical dissolution of pore walls by adsorbing and changing the double-layer structure at the oxide/electrolyte interface thus smoothing and increasing film thickness [47–51]. As earlier, it was demonstrated that oxalic acid additives affected the electrochemical oxidation process of aluminum in sulfuric acid solution, leading to thicker oxide layer formation and mechanical property improvement compared to the process in pure electrolytes [21, 47, 52]. Oxyanions changed the morphology of the anodic films, making them more compact, less porous, and more corrosion-resistant. It was also shown that molybdate additions increased the AA thickening rate during anodizing in sulfuric acid or the mixture of sulfuric and tartaric acids [48, 50, 52, 53]. In our previous studies, we used formic acid anodizing with ammonium heptamolybdate and oxalic acid additives as an effective method for forming carbon-enriched composite products, i.e. the average carbon content was almost twice as much as in the oxalic and tartaric acid alumina films. At the same time, the anodizing voltage was 80 V, which is comparable with the anodizing voltage in oxalic acid and 2.5 times lower than in tartaric acid. This is important for reducing energy consumption when producing carbon-enriched AA films. The properties of the carbon-enriched AA strongly depend on the composition, textural characteristics, morphology, and the state and form of carbon-containing inclusions [54–56]. Therefore, in the present study, we continue our research and first try to determine the effect of ammonium heptamolybdate and oxalic acid additives, as well as formic acid concentration, on the composition, morphology, and FL of the AA films. Then, as carbon-containing species are incorporated into the alumina matrix and can interact with it, it is worth extracting and studying the carbon-containing component from films obtained in different conditions.

2. Experimental

2.1. Synthesis of the AA films and carbon-containing component extraction

All samples were prepared using high-purity aluminum foil (99.99 wt. %, 100 μm thick, 20 × 20 mm, AlfaAesar). The aluminum surface was pretreated in a hot solution of 1.5 M NaOH for 30 s, neutralized in 1.5 M HNO₃ for 2 min, then carefully rinsed in distilled water and air-dried. The one-sided anodizing was carried out in the aqueous solution of 0.4 M formic acid containing (1) 0.03 M (NH₄)₆Mo₇O₂₄ (pH 3.1) and (2) 20 mM H₂C₂O₄ (pH 1.65) in the thermostated two-electrode Teflon electrochemical cell (250 ml) at

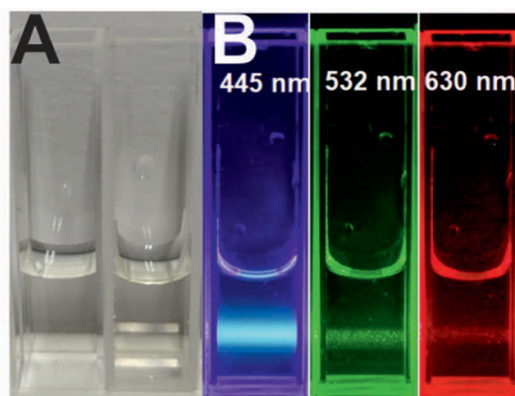


Figure 1. The final solutions of dissolved in 0.1 M HCl (ca. 100 °C) AA films obtained in 0.4 M HCOOH + 0.03 M $(\text{NH}_4)_6\text{Mo}_7\text{O}_{24}$ and 0.4 M HCOOH + 20 mM $\text{H}_2\text{C}_2\text{O}_4$ under natural light (A) and laser irradiation (B): 445 nm (blue), 532 nm (green), and 630 nm (red).

80 V, 18 °C, 1 h. The platinum grid was used as a counter electrode. AA films were also formed in 0.8 M HCOOH + 0.03 M $(\text{NH}_4)_6\text{Mo}_7\text{O}_{24}$ (pH 1.7) at 80 V, 18 °C, 1 h, and in 1.8 M H_2SO_4 at 18 V, 18 °C, 2 h. The temperature of the solutions was maintained using a cryostat Lauda (WK 230). The anodizing process was controlled by a direct current power supply GW Instek (GPR-30H100). A Viton O-ring set out the anodizing area of ca. 1.67 cm². Aluminum was chemically etched in the solution containing CuCl_2 and HCl to obtain free-standing alumina films (without Al substrate).

To extract the carbon-containing component from the samples, we dispersed the anodic alumina films formed in different electrolytes and dissolved them in a hot (ca. 100 °C) aqueous solution of 0.1 M HCl. The obtained solutions are transparent or slightly yellowish. Under laser irradiation (445 nm (blue), 532 nm (green), and 630 nm (red)), the Tyndall effect was observed. Moreover, all samples possessed strong greenish FL under blue laser exposure (figure 1), indicating the presence of nanosized particles in solutions.

As known, formic acid AA, besides alumina and water, also contains amorphous carbon inclusions. Therefore, when the films are dissolved in HCl, Al^{3+} and Cl^- ions and carbon-containing species are formed in the solutions. It is logical to assume that in an acidic medium, only carbon-containing species may exist as nanoparticles, namely, as carbon nanoparticles (CNPs). Thus, by combining with the surface groups of CNPs, metal ions can affect the properties of the CNPs. So, it was shown that Al^{3+} and Fe^{3+} ions became one of the most effective sources among other metal ions for quenching the FL of the CNPs [57]. Therefore, the solutions were carefully washed from Al^{3+} ions by dialysis in SnakeSkin® 10 kDA for 24 h, centrifugated (Fisherbrand, 7000 rpm, 5 min), and filtrated (Q-Max® RR Syringe Filters 13 mm, 0.45 μm PTFE, hydrophobic). The pH of the final solutions was ca. 5–6. The solutions of CNPs obtained from the AA films formed in 0.4 M HCOOH + 0.03 M $(\text{NH}_4)_6\text{Mo}_7\text{O}_{24}$ and 0.4 M HCOOH + 20 mM $\text{H}_2\text{C}_2\text{O}_4$ are denoted CNPs-1 and CNPs-2, respectively.

2.2. Characterization

The morphology of the films was investigated by scanning electron microscopy (SEM) using a scanning electron microscope FEI Quatra 200F. The microscope was equipped with a field emission gun, the voltage was 2 keV (low voltages needed due to charge accumulation on the surface of non- or low- conductive samples), and the samples were placed in a chamber with a pressure of 2×10^{-5} mbar. To determine the content of carbon entrapped in the anodic film, thermogravimetry (TG)/differential thermal analysis (DTA) coupled with mass spectrometry (MS) of evolved H_2O , CO_2 , and CO gases were applied. The simultaneous thermal analysis apparatus STA Pt 1600 (Linseis, Selb, Germany) was used with the mass spectrometer MS Thermostar GDS 320 (Linseis/Pfeiffer, Asslar, Germany). For the investigation, 19–22 mg of the sample was loaded in Al_2O_3 crucibles and then heated in an argon (Ar 6.0) atmosphere up to 1300 °C at a heating rate of 10 °C min⁻¹. The data were collected and fitted using the software provided with the equipment.

The optical properties of the anodic alumina films and CNP aqueous solutions were studied by UV–Vis absorption spectroscopy (JASCO V-670, JASCO Ltd, Japan) and FL spectroscopy (FS5, Edinburgh Instruments Ltd, UK) using 1 cm path-length quartz cuvettes. The absorbance spectra were recorded in the 200–700 nm range with a 0.5 nm resolution and a speed of 200 nm min⁻². CNP concentrations were low enough to avoid the self-absorption effect with an absorbance value not exceeding ca. 0.2. For FL measurements, samples were excited by the 150 W CW Ozone-free Xenon arc lamp at $\lambda_{\text{ex}} = 260\text{--}450$ nm. FL spectra were recorded at 350–650 nm spectral range with 0.3 nm and 0.2 nm slit for excitation and emission,

respectively. The measurement error did not exceed 1%–2%. All measurements were carried out at room temperature, and FL spectra were corrected for instrument sensitivity.

FL time-decay kinetics were measured using time-resolved FL spectroscopy (FL920, Edinburgh Instruments Ltd, UK) under 375 nm picosecond laser diode excitation with pulse duration 57.3 ps, repetition rate of 5 MHz (200 ns), pulse power 140 μ W. The FL decay kinetics were approximated using three-component exponentials considering the instrumental function with different characteristic decay times. The fitting procedure was done using Edinburgh F920 advances lifetime analysis software package. The goodness-of-fit parameter (χ^2) was around 1.

The size distribution of CNPs was characterized by transmission electron microscopy (TEM, LEO-906E, Leica Microsystems GmbH, Germany). The surface charge was estimated by Zetasizer Nano ZS (Malvern Instr.) Data were analyzed using Malvern Zetasizer software 7.03. Surface-enhanced Raman scattering (SERS) spectroscopy was performed using a Renishaw InVia Raman (United Kingdom) spectrometer equipped with a thermoelectrically cooled (-70 °C) CCD camera and microscope. The continuous wave He-Cd Kimmon (Japan) laser emitting 442 nm wavelength light was used for the excitation via Leica 50 \times /0.75NA objective. Spectra were corrected using polynomial function background subtraction, and a binomial smoothing procedure was applied to the experimental data using the GRAMS/AI 8.0 (Thermo Electron Corp.) software. Carbon-containing residuals were detected using silver nanoparticles (AgNPs) obtained by the previously described method [58]. The samples were mixed with AgNPs in a ratio of 5:1, applied on a stainless steel 'Tienta' substrate for Raman, and dried at room temperature. The procedure was repeated two times. Then, the samples were washed with Milli-Q water to remove the salts from sample solutions and impurities from the synthesis of the AgNPs.

2.3. Biocompatibility assay

COS-7 cells (Cell line service, product number 605470) were grown in Ibidi high 8-well plate (Ibidi, catalog number: 80806) in DMEM medium (Gibco, catalog number: 31053028), supplemented with 10% fetal bovine serum (FBS) (Gibco, catalog number: A3840102) and Penicillin-Streptomycin (Gibco, catalog number: 15140122). $2.5 \cdot 10^4$ cells per well were seeded on the first day and grown in an incubator at 37 °C 5% CO₂. After 2 d, cells were washed 3 times with PBS (Gibco, catalog number: 10010023) and incubated with different concentrations of Qdots at 37 °C 5% CO₂, which were diluted in FluoroBrite DMEM medium (Gibco, catalog number: A1896701) supplemented with 10% FBS, Penicillin-Streptomycin and GlutaMAX (Gibco, catalog number: 35050061). Before adding to the glass coverslip-adhered cells, all CNP stock solutions were filtered using a syringe filter containing 0.1 μ m-sized pores (Whatman, catalog number: 6809-1012). Bright-field microscopy images of control and CNP-treated COS-7 cells were acquired at room temperature using a ZEISS Primovert inverted microscope equipped with ZEISS AxioCam ERc 5 s camera and using a 10X objective, which is supplied as a pre-installed objective in the microscope's body. For the cell viability measurements, COS-7 cells, either untreated or incubated with respective concentrations of CNPs-1 or CNPs-2, after 10 h of overall incubation time, were initially washed 1 time with PBS (Gibco, catalog number: 10010023) and treated with 1X TrypLE Express (Gibco, catalog number: 12604013) for 5 min at 37 °C 5% CO₂. Then, the enzyme was inactivated by adding FluoroBrite DMEM medium (Gibco, catalog number: A1896701) into the wells, and the detached cells were centrifuged for 5 min at 200 g. After centrifugation, the cell pellet was resuspended in 100 μ l DMEM medium (Gibco, catalog number: 31053028), and 10 μ l of the cell suspension was mixed with Trypan Blue Stain (Invitrogen, catalog number: T10282) to obtain a final 0.2% (v/v) concentration of the dye. Such samples were then analyzed using Countess II Automated Cell Counter that enabled the quantification of viable cells.

3. Results and discussion

According to SEM studies, the AA films formed in electrolytes containing 0.4 M or 0.8 M HCOOH and 0.03 M (NH₄)₆Mo₇O₂₄ have a dense, cracked cover layer on the surface and hexagonal-shaped cells on the back side (i.e. anodizing front) (figures 2(A), (D) and (B), (E)). The average cell size does not depend on the formic acid concentration and is about 180 nm, resembling the porous structure of the films. SEM observations of the sample back sides also reveal a highly wavy Al|Al₂O₃ interface. The degree of back-side inhomogeneity depends on the formic acid concentration and becomes more pronounced with increasing acid concentration. Thus, the thickness of the film formed in 0.4 M HCOOH + 0.03 M (NH₄)₆Mo₇O₂₄ is 15.20 μ m and practically does not change throughout the sample (figure 2(C)). However, the surface and back sides are highly wavy for Al anodizing in 0.8 M HCOOH + 0.03 M (NH₄)₆Mo₇O₂₄, and film thickness varies from 31.25 to 51.78 μ m (figure 2(F)). It should be noted that usually, during porous Al anodizing in most electrolytes, the AA layer has the same thickness, the surface has a highly ordered porous structure, and the back side is also ordered and uniform. When the oxalic acid is added to the formic acid solution, the

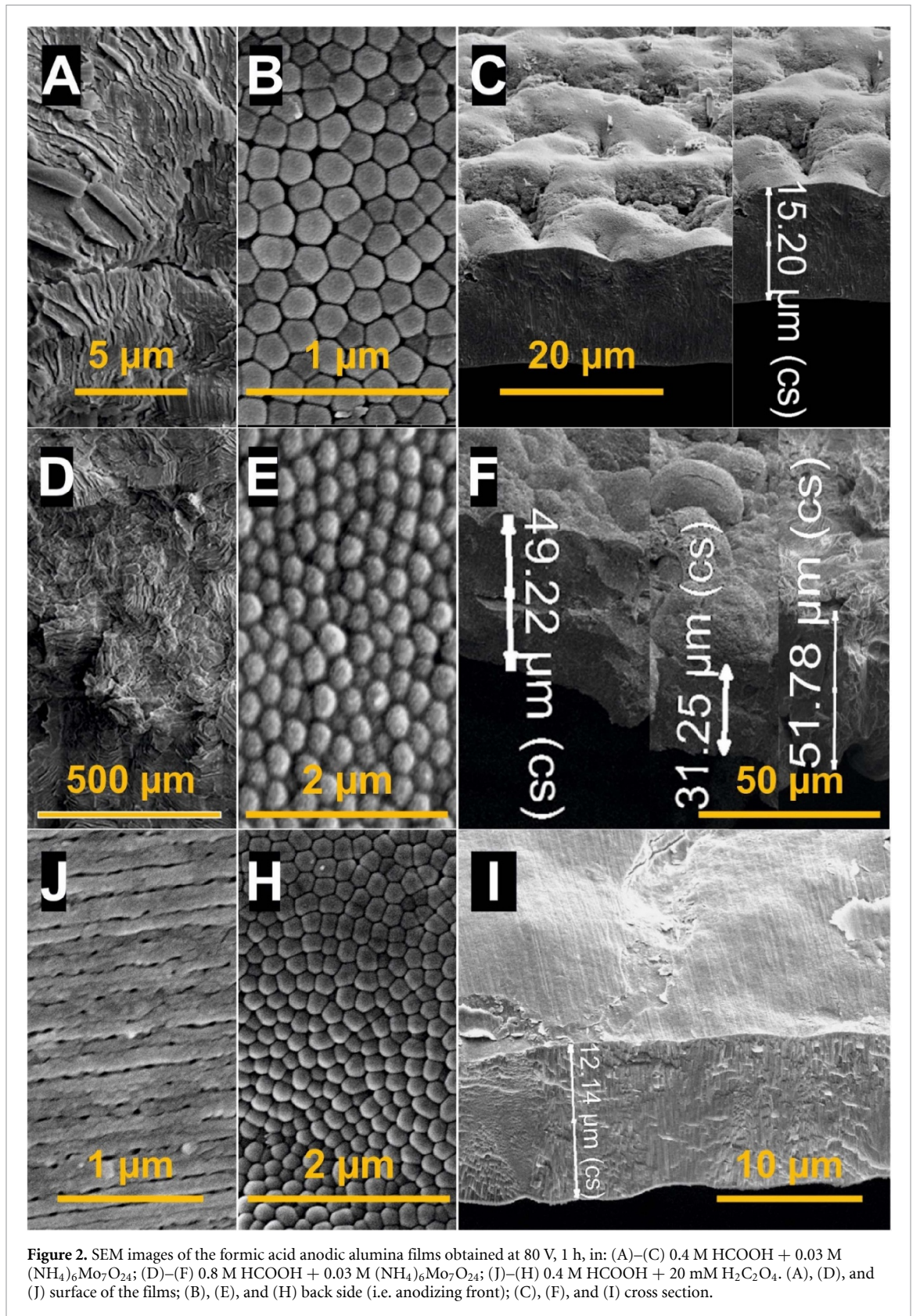


Figure 2. SEM images of the formic acid anodic alumina films obtained at 80 V, 1 h, in: (A)–(C) 0.4 M HCOOH + 0.03 M $(\text{NH}_4)_6\text{Mo}_7\text{O}_{24}$; (D)–(F) 0.8 M HCOOH + 0.03 M $(\text{NH}_4)_6\text{Mo}_7\text{O}_{24}$; (J)–(H) 0.4 M HCOOH + 20 mM $\text{H}_2\text{C}_2\text{O}_4$. (A), (D), and (J) surface of the films; (B), (E), and (H) back side (i.e. anodizing front); (C), (F), and (I) cross section.

situation changes: the film surface becomes porous (dense, cracked cover layer disappears), the cell size slightly decreases (ca. 170 nm), and the film thickness also decreases to 12.14 μm and almost loses its wavy structure (figures 2(J) and (I)).

As was shown in our previous TG/DTA and FTIR studies, carbon-containing inclusions are in the form of CO_2 , CO, carboxylate ions, and amorphous carbon ($a\text{-C:H}$) [55, 56]. Moreover, the amount of carbon associated with amorphous carbon was determined. According to table 1, the formic acid concentration does

Table 1. Carbon content (mass%) in the anodic alumina films formed in 0.4 M HCOOH (FA) + 0.03 M (NH₄)₆Mo₇O₂₄ (AHM), 0.8 M HCOOH + 0.03 M (NH₄)₆Mo₇O₂₄, and 0.4 M HCOOH + 20 mM H₂C₂O₄ (OxA) at 80 V according to TG/DTA/MS data.

Sample	ω_C , % (<i>a</i> -C:H)	ω_C , % (total)
0.4 M FA + 0.03 M AHM	3.7	5.3
0.8 M FA + 0.03 M AHM	3.3	5.0
0.4 M FA + 20 mM OxA	3.2	3.4

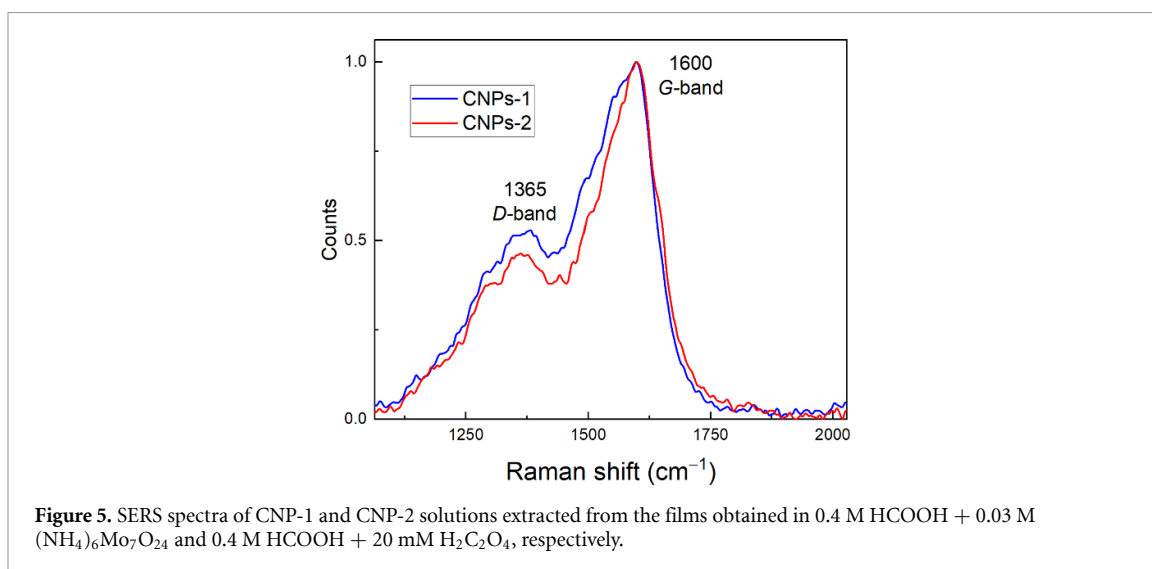
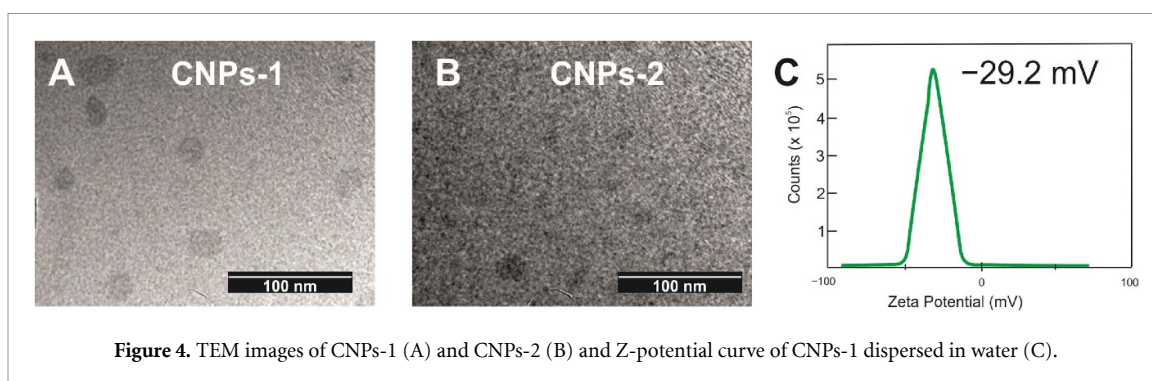
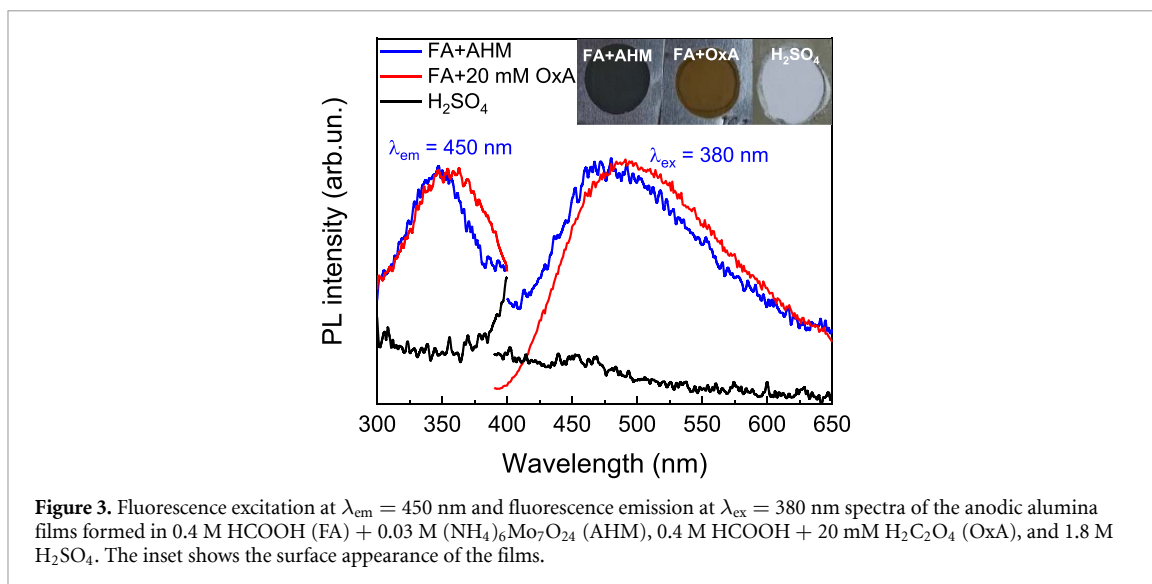
not significantly affect the total carbon content in the films if the electrolyte contains ammonium heptamolybdate, 5.3 mass% versus 5.0 mass% for 0.4 M and 0.8 M formic acid solutions, respectively. If only oxalic acid is added to the formic acid, the total carbon content is lower and equals 3.4 mass%. However, the *a*-C:H content varies slightly between different samples: 3.7 mass% for 0.4 M HCOOH + 0.03 M (NH₄)₆Mo₇O₂₄; 3.3 mass% for 0.8 M HCOOH + 0.03 M (NH₄)₆Mo₇O₂₄; 3.2 mass% for 0.4 M HCOOH + 20 mM H₂C₂O₄, which means that regardless of the electrolyte composition, the conversion degree of formate ions into *a*-C:H is constant. At the same time, the amount of CO₂, CO, and carbonate-carboxylate species may vary depending on the electrolyte composition. Generally, impurities are not homogeneously distributed through the film thickness. In the case of carbon-containing electrolytes, carbon concentration is higher in the outer layer and constant in the inner layer [10, 59]. Therefore, the number of formate ions penetrating the oxide does not change. However, the number of formate ions converted into CO₂, CO, and carbonate-carboxylate ions varies, which explains the difference in the total carbon amount in our samples.

Differences in the morphology of the films can also be explained by the effects of oxalic acid and ammonium heptamolybdate on the Al anodizing in formic acid solutions [48, 50, 52, 53, 60]. The behavior of oxyanions, e.g. molybdates, in acidic media is complex. Molybdates are polymeric in the solutions with pH < 4.5 [61]. Various molybdenum oxides of the following H_xMoO₃, 0 < x < 2, are produced during Al anodizing [48, 53]. These different electrolyte elements are incorporated at the electrolyte/oxide interface and inhibit the transfer of aluminum cations to the electrolyte thus increasing the rate of porous layer growth and decreasing the diameter of pores [48, 50, 53]. In contrast, oxalic acid does not prevent the transfer of Al³⁺ ions to the solution, but it also prevents pitting corrosion of alumina at the initial stages of Al anodizing in formic acid [47, 52, 54, 62].

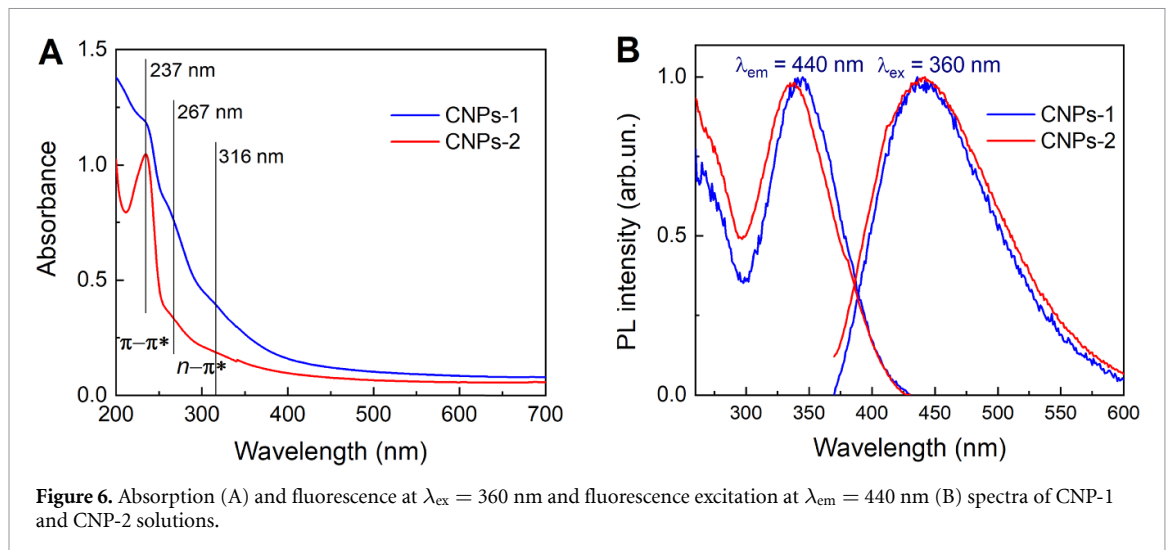
To study the FL properties of samples containing carbon and those without carbon, we obtained the sulfuric acid AA films. The first thing to note is the differences in the colors of the samples obtained. The ones formed in formic-acid-containing solution are black (0.4 M HCOOH + 0.03 M (NH₄)₆Mo₇O₂₄) or yellowish (0.4 M HCOOH + 20 mM H₂C₂O₄), and the ones formed in sulfuric acid are colorless and completely transparent (figure 3, Inset). The color of the samples is related to the amount of carbon-containing embedded in the anodic alumina (see table 1). Second, the FL excitation spectra of both samples formed in formic-acid-containing electrolyte ($\lambda_{em} = 450$ nm) have a narrow peak (FWHM is ca. 60 nm) in the wavelength range of 300–400 nm with a maximum at ca. 350 nm; the emission spectra of these films ($\lambda_{ex} = 380$ nm) have a broad emission peak (FWHM is ca. 125 nm) in the wavelength region of 400–650 nm with a maximum at ca. 490 nm. However, the sulfuric acid AA films do not have a detectable FL in the mentioned wavelength regions (see figure 3). Thus, we can conclude that the FL in the 400–650 nm region is due to carbon-containing inclusions in the formic acid AA.

The carbon component was extracted from AA films, and as already mentioned, we obtained the aqueous solutions of CNPs (section 2.1). Figures 4(A) and (B), shows the TEM images of the obtained CNPs, revealing the spherical separated from each other nanoparticles with a ca. 20–25 nm diameter. The zeta potential of the CNP-1 and CNP-2 solutions does not differ and shows a single negative peak at –29.2 mV with a width of 8.20 mV (figure 4(C)). The negative potential indicates that the surface of CNPs has negatively charged moieties, such as C=O, C–O, and O–H, which are essential to get the water solubility of CNPs. Z-potential also shows the degree of repulsion between the charged particles in the dispersion. High zeta potential implies highly charged particles, which prevents aggregation of the particles due to electric repulsion. If the zeta potential is low, attraction overcomes repulsion, and the mixture likely coagulates. The zeta-potential value of –30 mV is considered optimum for good stabilization of a nanodispersion [63]. Therefore, in our case, the value of zeta-potential indicates that the colloidal stability of CNPs is high, and the solutions can be used over time.

SERS spectra of CNPs-1 and CNPs-2 obtained from the films formed in the solution of 0.4 M HCOOH + 0.03 M (NH₄)₆Mo₇O₂₄ and 0.4 M HCOOH + 20 mM H₂C₂O₄, respectively, show two distinct peaks at 1365 cm^{–1} (*D*-band) and 1600 cm^{–1} (*G*-band) (figure 5). The intensity ratio of the peak of the *G*- to the *D*-band was found to be 2.20.



The G-band (sp^2 hybridization) represents the graphitization degree associated with the CNPs, and the D-band (sp^3 hybridization) represents the amount of defect and functionalization. The I_G/I_D ratio indicates that the synthesized CNPs mainly comprise sp^2 graphitic carbons with sp^3 carbon defects originating from oxygen-containing groups [64–67] that agree with the negative surface charge of the nanoparticles. SERS results agree with Raman spectra of CDs obtained by other methods [66, 68]. Moreover, our FTIR studies of the corresponding films [55] and films formed in tartaric acid [69] confirm that amorphous carbon is linked to the oxide network through the carboxylate ions and coordinative polyhedra of Al^{3+} ions.



UV-Vis absorption spectra of the CNP-1 and CNP-2 solutions have characteristic bands at 237, 267, and 316 nm and a long absorption slope toward 500 nm (figure 6(A)). The typical absorption spectrum of CDs, like CNPs, appears as a strong absorption in the UV region (230–320 nm), sometimes with a band at 285 or 340 nm and a long tail expanding in the visible region, which partly belongs to the light scattered on the small particles [64–68]. The absorption in the 230–290 nm region belongs to the $\pi-\pi^*$ transitions in the C=C bonds, and in the 290–380 nm region, to the $n-\pi^*$ transitions usually determined by C=O bonds or other species outside the core-shell [65]. As well as anodic alumina films formed in formic-acid-containing electrolytes (see figure 3), CNP-1 and CNP-2 solutions possess similar FL.

The FL excitation spectra of both CNP samples ($\lambda_{\text{em}} = 440$ nm) have a similar narrow peak (FWHM of ca. 60 nm) at ca. 350 nm (figure 3). Upon excitation at 360 nm, the CNP spectra exhibit one broad and strong emission band at ca. 440 nm (figure 6(B)). Our results agree with the ones existing in the literature. So, similar absorption-emission features were observed for carbon dots (CDs) obtained using different techniques [57, 70, 71]. Compared with the FL spectra of the source AA films, the emission spectra of the CNPs are narrower, with a maximum blueshifted to 440 nm. It can be explained by the effect of the alumina matrix, which is also amorphous and has various structural and point defects, contributing to the total emission of the samples and affecting the shape and maximum position of the FL spectra [31, 37, 40, 42, 72, 73].

Solutions of CNPs-1 and CNPs-2 exhibit an excitation-dependent emission behavior at 280–450 nm excitation wavelengths. At $\lambda_{\text{ex}} = 280$ –290 nm, the emission maximum is at ca. 450 nm, and it slightly blueshifts to 415 nm at $\lambda_{\text{ex}} = 320$ –340 nm. It redshifts from 415 to 525 nm as λ_{ex} increases from 350 to 450 nm (figure 7). The excitation-dependent emission behavior is one of the typical photophysical characteristics of CDs that originates from the surface state of these nanomaterials [57, 64, 70, 74–77]. The bandgap of CDs decreases with an increase in the degree of oxidation, i.e. CDs with a lower degree of oxidation are more likely to be excitation-independent [71]. At least two FL mechanisms for CDs are extensively accepted. One mechanism is that the FL comes from the band gap states based on the conjugated π -domains in the carbon nucleus of the CDs, and the other is that the luminescence comes from the surface-related defect band states of the CDs, which can cause surface energy traps [75]. In our case, both mechanisms are involved: the first dominates when the core of CNPs is excited at $\lambda_{\text{ex}} = 300$ –340 nm, and the second appears due to various emission centers, such as carbonyl, carboxyl, and hydroxyl groups on the CNPs surface, under 280–300 nm and 340–450 nm excitation.

Time-resolved FL experiments are performed at $\lambda_{\text{ex}} = 375$ nm to observe the pure radiative recombination processes as a necessary complement. All the FL transients are probed at FL peaks and are well-fitted with multi-exponential functions. The best-fit parameters are listed in table 2; results for the anodic alumina films are shown for comparison. For the anodic alumina films, the average FL lifetimes (τ_{ave}) do not depend on the anodizing conditions and are 1.54 and 1.59 ns for samples formed in 0.4 M HCOOH + 0.03 M $(\text{NH}_4)_6\text{Mo}_7\text{O}_{24}$, 0.4 M HCOOH + 20 mM $\text{H}_2\text{C}_2\text{O}_4$, respectively. For the CNP solutions, τ_{ave} significantly increases compared with the films and are 7.25 and 8.04 ns for CNPs-1 and CNPs-2, respectively. In our previous works [8, 55, 78], it is shown that AA films obtained in different organic acids have similar FL spectra in the 400–700 nm wavelength region and FL decay times of 0.3–3.1 ns. Therefore, increased τ_{ave} of CNPs compared with τ_{ave} for the films indicates that the AA film matrix quenches the FL of

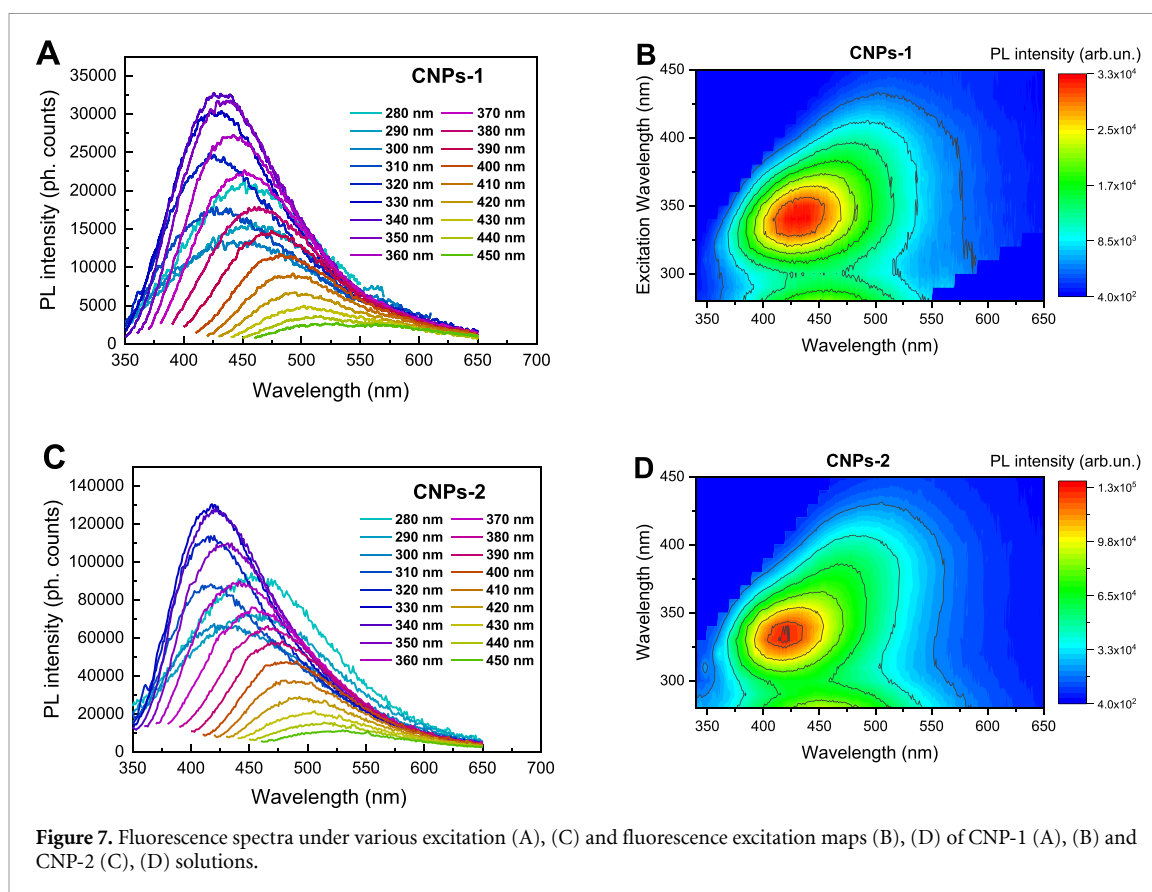


Figure 7. Fluorescence spectra under various excitation (A), (C) and fluorescence excitation maps (B), (D) of CNP-1 (A), (B) and CNP-2 (C), (D) solutions.

Table 2. Decay times determined for anodic alumina films formed in 0.4 M HCOOH + 0.03 M $(\text{NH}_4)_6\text{Mo}_7\text{O}_{24}$, 0.4 M HCOOH + 20 mM $\text{H}_2\text{C}_2\text{O}_4$ and solutions of CNPs-1 and CNPs-2 ($\lambda_{\text{ex}} = 375$ nm).

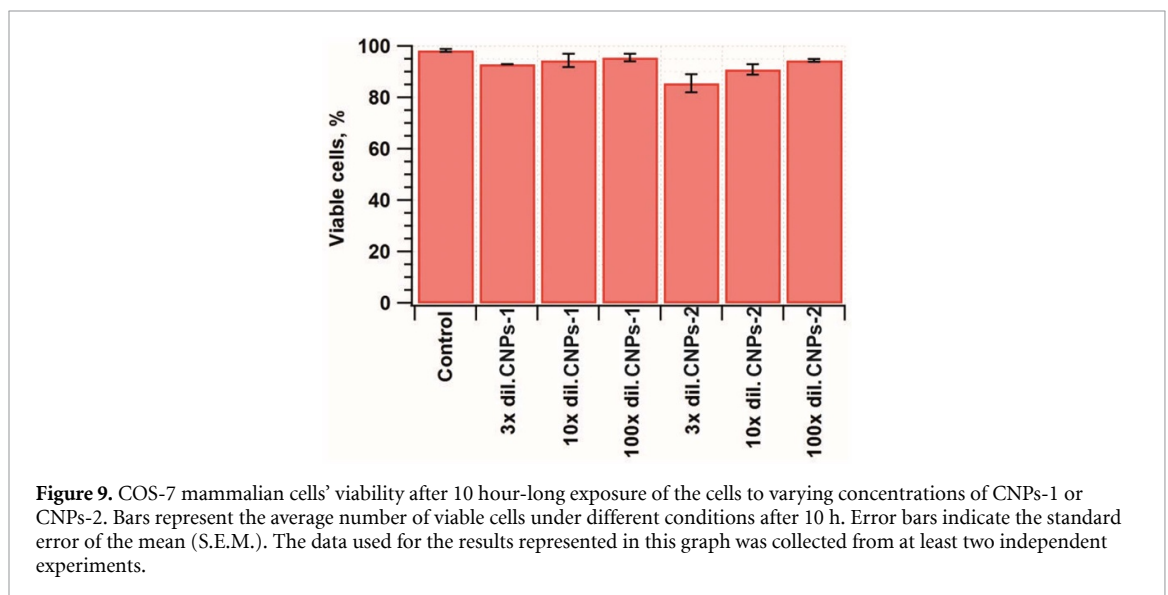
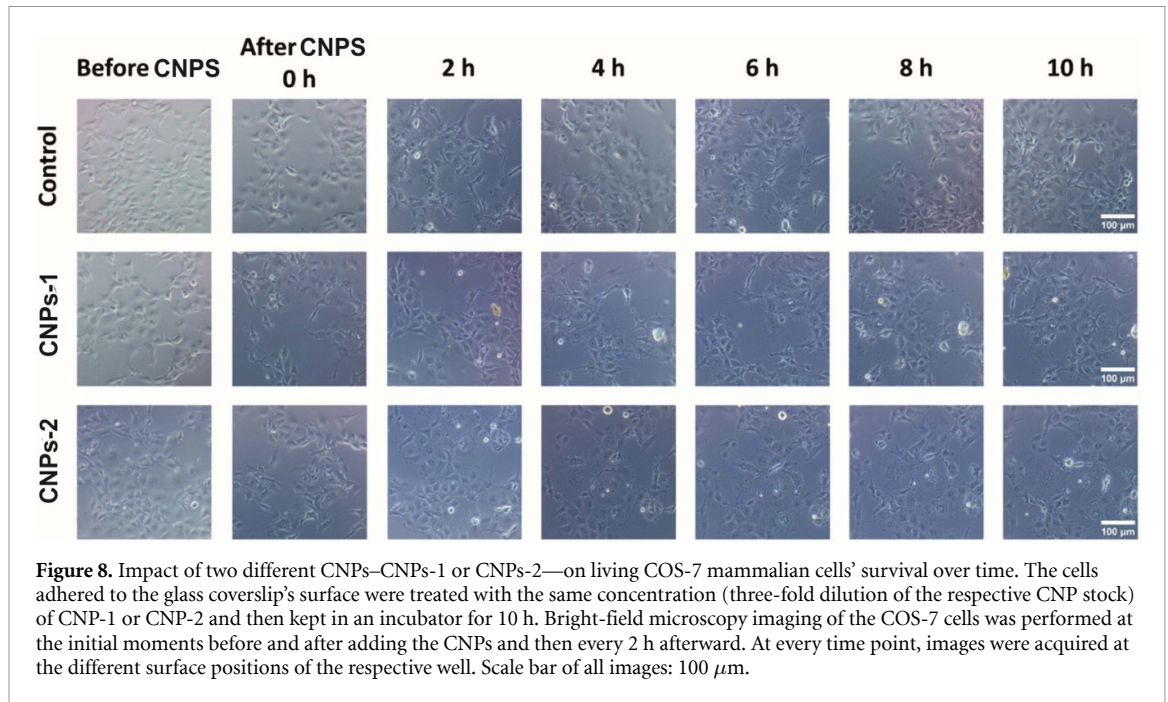
Sample	FL excitation band, nm	FL band, nm	τ_1 , ns (%)	τ_2 , ns (%)	τ_3 , ns (%)	τ_{ave} , ns
FA + AHM	347	484	0.16 (25%)	0.80 (41%)	3.4 (34%)	1.54
FA + 20mM OxA	355	490	0.10 (17%)	0.71 (42%)	3.1 (41%)	1.59
CNPs-1	343	440	0.50 (11%)	2.71 (34%)	11.4 (55%)	7.25
CNPs-2	337	440	0.64 (11%)	3.06 (34%)	12.6 (55%)	8.04

the carbon-containing inclusions by approximately five times (see table 2). Our present results also prove the hypothesis that the origin of FL (400–700 nm) in the AA films is mainly due to carbon-containing inclusions.

FL decay of electrochemically and solvothermally synthesized CNPs is also nonexponential and can be decomposed into three components [70]. However, in our case, τ_{ave} are longer (ca. 0.1 ns and 2.5 ns for electrochemically and solvothermally synthesized CNPs, respectively) and comparable with those of hydroxyl-coated CNPs (9.5 ns) [57]. This indicates the radiative recombination nature of excitations in our samples. Since in most carbon nanomaterials, the surface states with functional groups are disordered and mainly depend on synthesis and post-treatment conditions, the difference in τ_{ave} can be explained not only by the presence of various functional groups on the surface of CNPs but also by a higher degree of purification [57, 79–81].

Since the CNPs were obtained by the dissolution of anodic alumina films without additional treatment, such as ultrasonication, we can conclude that, first, carbon-containing species obtained during the anodic oxidation of formate ions are incorporated in the alumina in the form of amorphous carbon that can be extracted from the initial films. Second, these carbon-containing species are luminescent carbon nanoparticles; third, the alumina matrix significantly quenches the FL of the embedded carbon.

As is known, the CNPs could be exceptional candidates for detection technology due to chemical and biological compatibility, well-defined luminescence signal with tunable wavelength options, diverse surface functionality for further modification, low electrical resistance, and acceptable conductivity. Several designed detecting systems are also constructed around CNP luminescence signals measuring a diverse range of analytes in biological environments [77, 82, 83]. Therefore, to test whether our novel CNPs confer cytotoxicity, we performed their biocompatibility assay with living COS-7 mammalian cells. For this purpose, three different concentrations (3-fold, 10-fold, and 100-fold dilution of the stock solution) of



respective CNPs were introduced into the wells containing glass surface-adhered living COS-7 cells and; after that, the samples were stored in an incubator for 10 h with the repeating bright-field microscopy imaging cycles every 2 h. Even at the highest concentration, CNPs-1 and CNPs-2 had little to no effect on both COS-7 cells' morphology and surface adhesion properties observed after 10 h of incubation (figure 8).

The negative impact of only a minimal extent to the living cells was also confirmed by assessing the number of viable COS-7 cells left at the very end of the experiment (after 10 h), as for three-fold diluted CNPs-1 93 ± 0% of the cells remained viable and for three-fold diluted CNPs-2 the cell survival index was 85.8 ± 3.5%, while for the CNP untreated cells this value was estimated to be 98.3 ± 0.5% (figure 9).

Therefore, we conclude that CNPs-1 and CNPs-2 exhibit high biocompatibility and can possibly be used for various *in vivo* applications with negligible harm to the living cells' integrity. However, if our method for synthesizing carbon nanoparticles from carbon-containing anodic alumina is considered a new and promising way, it should be improved, and further research is needed. It can be done in one of the following ways: by improving the synthesis conditions of the initial films to obtain samples with a larger amount of carbon and with a smaller CNP size for their more effective use in luminescence-based immunoassays. Depending on the procedure and degree of purification of CNPs and the pH of their solutions, the luminescent properties of the particles can also be improved.

4. Conclusions

SEM studies established that anodic alumina films formed in electrolytes containing 0.4 M/0.8 M HCOOH and 0.03 M $(\text{NH}_4)_6\text{Mo}_7\text{O}_{24}$ have a dense, cracked cover layer on the surface and hexagonal-shaped cells on the back side (i.e. anodizing front). The average cell size does not depend on the formic acid concentration and is about 180 nm, resembling the porous structure of the films. However, the oxalic acid additives change the situation: the film surface becomes porous (dense, cracked cover layer disappears), and the cell size slightly decreases (ca. 170 nm). DTA/DG studies coupled with mass spectroscopy showed that the total carbon content in the films does not depend on the formic acid concentration (5.0–5.3 mass%) but depends on the electrolyte composition (3.4 mass% for formic acid anodizing with oxalic acid additives). However, the amorphous content varies slightly between different samples: 3.7 mass% for 0.4 M HCOOH + 0.03 M $(\text{NH}_4)_6\text{Mo}_7\text{O}_{24}$; 3.3 mass% for 0.8 M HCOOH + 0.03 M $(\text{NH}_4)_6\text{Mo}_7\text{O}_{24}$; 3.2 mass% for 0.4 M HCOOH + 20 mM $\text{H}_2\text{C}_2\text{O}_4$. Regardless of the electrolyte composition, the conversion degree of formate ions into *a*-C:H is constant.

The obtained films have a wide blue FL in the wavelength range of 400–650 nm with a maximum at around 490 nm. It was determined that carbon-containing impurities are responsible for the FL properties of the films as samples obtained in sulfuric acid (i.e. without carbon) do not possess detectable FL in the mentioned wavelength region. The FL decay is nonexponential and has an average lifetime of 1.54 and 1.59 ns for ammonium heptamolybdate and oxalic acid, respectively. The FL spectrum is a superposition of several decay components.

The carbon-containing species obtained during the aluminum anodic oxidation in formic acid with ammonium heptamolybdate or oxalic acid additives were extracted by film dissolution and then characterized. It was shown that the solutions contain carbon nanoparticles with a diameter of 20–25 nm. SERS revealed that the synthesized CNPs mainly comprise sp^2 graphitic carbons with sp^3 carbon defects originating from oxygen-containing groups that agree with the negative surface charge of the nanoparticles. Carbon nanoparticle solutions exhibit an excitation-dependent emission behavior at 280–450 nm excitation wavelengths with average lifetimes of 7.25–8.04 ns, depending on the composition of the initial film. Increased average lifetimes compared with the initial films indicate that the alumina matrix significantly decreases the FL effectiveness of the embedded CNPs. Since the CNPs were obtained by the dissolution of anodic alumina films without additional treatment, such as ultrasonication, we can conclude that amorphous carbon can be obtained during the anodic oxidation of formates. Time-resolved FL measurements revealed that the alumina matrix significantly decreases the FL effectiveness of the embedded carbon nanoparticles.

Carbon nanoparticle FL is caused by the core of CNPs at $\lambda_{\text{ex}} = 300\text{--}340$ nm and by various emission centers on their surface, such as carbonyl, carboxyl, and hydroxyl groups, under 280–300 nm and 340–450 nm excitation. As CNPs could be exceptional candidates for detection technologies, the biocompatibility assays were performed with living COS-7 mammalian cells, showing a minimal negative impact on the living cells.

Data availability statement

All data that support the findings of this study are included within the article (and any supplementary files).

Acknowledgments

This work was partially supported by Horizon Europe FLORIN (Project No. 101086142) and the Research Council of Lithuania (Grant No. S-MIP-23-70).

ORCID iDs

Katsiaryna Chernyakova  <https://orcid.org/0000-0002-6616-4353>
Ieva Matulaitienė  <https://orcid.org/0000-0001-7664-2331>
Tatjana Charkova  <https://orcid.org/0000-0002-2043-9024>
Giedrė Grincienė  <https://orcid.org/0000-0002-9830-6301>
Meda Jurevičiūtė  <https://orcid.org/0000-0002-5754-8603>
Aurimas Kopūstas  <https://orcid.org/0000-0002-2972-1851>
Arūnas Jagminas  <https://orcid.org/0000-0003-0191-8588>
Renata Karpicz  <https://orcid.org/0000-0001-5884-4538>

References

- [1] Galaburda M V, Bogatyrov V M, Tomaszewski W, Charmas B, Mischanchuk O V, Oranska O I, Gun'ko V M and Zybert M 2020 Synthesis and structural properties of carbon/alumina composites: practical application in solid phase extraction of explosives *Microporous Mesoporous Mater.* **300** 110159
- [2] Raut P, Dutta M, Sengupta S and Basu J 2013 Alumina-carbon composite as an effective adsorbent for removal of Methylene Blue and Alizarin Red-s from aqueous solution *Indian J. Chem. Technol.* **20** 15–20
- [3] Xu J, Wang A, Wang X, Su D and Zhang T 2011 Synthesis, characterization, and catalytic application of highly ordered mesoporous alumina-carbon nanocomposites *Nano Res.* **4** 50–60
- [4] Patil K C, Aruna S T and Mimani T 2002 Combustion synthesis: an update *Curr. Opin. Solid State Mater. Sci.* **6** 507–12
- [5] Vergunst T, Kapteijn F and Moulijn J 2002 Preparation of carbon-coated monolithic supports *Carbon* **40** 1891–902
- [6] Inagaki M, Kobayashi S, Kojin F, Tanaka N, Morishita T and Tryba B 2004 Pore structure of carbons coated on ceramic particles *Carbon* **42** 3153–8
- [7] Zhou J, Tang C, Cheng B, Yu J and Jaroniec M 2012 Rattle-type carbon–alumina core–shell spheres: synthesis and application for adsorption of organic dyes *ACS Appl. Mater. Interfaces* **4** 2174–9
- [8] Chernyakova K, Karpicz R, Zavadski S, Poklonskaya O, Jagminas A and Vrublevsky I 2017 Structural and fluorescence characterization of anodic alumina/carbon composites formed in tartaric acid solution *J. Lumin.* **182** 233–9
- [9] Jagminas A, Grincienė G, Selskis A and Chernyakova K 2019 Cleavage of alumina cells in organic acid solutions during high voltage anodization *Phys. Chem. Chem. Phys.* **21** 14941–4
- [10] Jagminas A, Klimas V, Chernyakova K and Jasulaitiene V 2022 Designing carbon-enriched alumina films possessing visible light absorption *Materials* **15** 2700
- [11] Magniez L, Tusch C D S, Fontana S, Cahen S, Martin J, Hérold C and Henrion G 2023 Plasma electrolytic oxidation of aluminium in electrolytes containing various concentrations of carbon black nanoparticles *Surf. Coat. Technol.* **473** 129990
- [12] Thompson G E 1997 Porous anodic alumina: fabrication, characterization and applications *Thin Solid Films* **297** 192–201
- [13] Sulka G D 2008 Highly ordered anodic porous alumina formation by self-organized anodizing *Nanostructured Materials in Electrochemistry* (Wiley Online Books (Wiley)) pp 1–116
- [14] Sulka G D 2020 Introduction to anodization of metals *Nanostructured Anodic Metal Oxides: Synthesis and Applications* (Elsevier) pp 1–34
- [15] Li S Y, Liu Z L, Xiang G X and Ma B H 2022 Photoluminescence properties of anodic aluminium oxide films formed in a mixture of malonic acid and oxalic acid *Luminescence* **37** 1864–72
- [16] Vrublevsky I, Jagminas A, Hemeltjen S and Goedel W 2009 Behavior of acid species during heat treatment and re-anodizing of porous alumina films formed in malonic acid *J. Solid State Electrochem.* **13** 1873–80
- [17] Knörnschild G, Poznyak A A, Karoza A G and Mozalev A 2015 Effect of the anodization conditions on the growth and volume expansion of porous alumina films in malonic acid electrolyte *Surf. Coat. Technol.* **275** 17–25
- [18] Ono S, Saito M and Asoh H 2005 Self-ordering of anodic porous alumina formed in organic acid electrolytes *Electrochim. Acta* **51** 827–33
- [19] Kikuchi T, Yamamoto T, Natsui S and Suzuki R O 2014 Fabrication of anodic porous alumina by squaric acid anodizing *Electrochim. Acta* **123** 14–22
- [20] Wood G C, Skeldon P, Thompson G E and Shimizu K 1996 A model for the incorporation of electrolyte species into anodic alumina *J. Electrochem. Soc.* **143** 74–83
- [21] Giovanardi R, Fontanesi C and Dallabarba W 2011 Adsorption of organic compounds at the aluminium oxide/aqueous solution interface during the aluminium anodizing process *Electrochim. Acta* **56** 3128–38
- [22] Ono S and Asoh H 2021 A new perspective on pore growth in anodic alumina films *Electrochem. Commun.* **124** 106972
- [23] Mardilovich P P, Govyadinov A N, Mukhurov N I, Rzhvskii A M and Paterson R 1995 New and modified anodic alumina membranes part I. Thermotreatment of anodic alumina membranes *J. Membr. Sci.* **98** 131–42
- [24] Brudzisz A M, Giziński D and Stępniewski W J 2021 Incorporation of ions into nanostructured anodic oxides—mechanism and functionalities *Molecules* **26** 6378
- [25] Aman J N M, Wied J K, Alhusaini Q, Müller S, Diehl K, Staedler T, Schönherr H, Jiang X and Schmedt Auf der Günne J 2019 Thermal hardening and defects in anodic aluminum oxide obtained in oxalic acid: implications for the template synthesis of low-dimensional nanostructures *ACS Appl. Nano Mater.* **2** 1986–94
- [26] Roslyakov I V, Shirin N A, Evdokimov P V, Berekchiian M V, Simonenko N P, Lyskov N V and Napolskii K S 2022 High-temperature annealing of porous anodic aluminium oxide prepared in selenic acid electrolyte *Surf. Coat. Technol.* **433** 128080
- [27] Roslyakov I V, Kolesnik I V, Levin E E, Katorova N S, Pestrikov P P, Kardash T Y, Solovyov L A and Napolskii K S 2020 Annealing induced structural and phase transitions in anodic aluminum oxide prepared in oxalic acid electrolyte *Surf. Coat. Technol.* **381** 125159
- [28] Szwachta G, Białek E, Włodarski M and Norek M 2022 Structural stability and optical properties of 1D photonic crystals based on porous anodic alumina after annealing at different temperatures *Nanotechnology* **33** 455707
- [29] Han H, Park S-J, Jang J S, Ryu H, Kim K J, Baik S and Lee W 2013 In situ determination of the pore opening point during wet-chemical etching of the barrier layer of porous anodic aluminum oxide: nonuniform impurity distribution in anodic oxide *ACS Appl. Mater. Interfaces* **5** 3441–8
- [30] Feng S and Ji W 2021 Advanced nanoporous anodic alumina-based optical sensors for biomedical applications *Front. Nanotechnol.* **3** 678275
- [31] Stępniewski W, Norek M, Michalska-Domańska M, Nowak-Stępniewska A, Kaliszewski M, Chilimoniuk P, Bombalska A and Bojar Z 2014 Fabrication and luminescence of anodic alumina with incorporated vanadyl citrate chelate anions *J. Mater. Sci. Nanotechnol.* **1** 1–7
- [32] Pashchanka M and Cherkashinin G 2021 A strategy towards light-absorbing coatings based on optically black nanoporous alumina with tailored disorder *Materials* **14** 5827
- [33] Hashimoto H, Fujita Y, Yazawa K and Asoh H 2023 Effects of anion incorporation on the local structure of porous-type amorphous alumina prepared by anodization: NMR study of Al coordination numbers *Results Phys.* **44** 106177
- [34] Choudhari K S, Choi C-H, Chidangil S and George S D 2022 Recent progress in the fabrication and optical properties of nanoporous anodic alumina *Nanomaterials* **12** 444
- [35] Robertson J 2002 Diamond-like amorphous carbon *Mater. Sci. Eng. R* **37** 129–281

- [36] Lin C, Yu M, Cheng Z, Zhang C, Meng Q and Lin J 2008 Bluish-white emission from radical carbonyl impurities in amorphous Al_2O_3 prepared via the Pechini-type sol–gel process *Inorg. Chem.* **47** 49–55
- [37] Cantelli L, Santos J S, Silva T F, Tabacniks M H, Delgado-Silva A O and Trivinho-Strixino F 2019 Unveiling the origin of photoluminescence in nanoporous anodic alumina (NAA) obtained by constant current regime *J. Lumin.* **207** 63–69
- [38] Wang J, Vu K N, Abell A D, Santos A and Law C S 2023 Nanoporous anodic alumina-based iontronics: fundamentals and applications *J. Mater. Chem. C* **11** 9051–81
- [39] Santos A, Kumeria T and Losic D 2013 Optically optimized photoluminescent and interferometric biosensors based on nanoporous anodic alumina: a comparison *Anal. Chem.* **85** 7904–11
- [40] Li Z J and Huang K L 2007 Optical properties of alumina membranes prepared by anodic oxidation process *J. Lumin.* **127** 435–40
- [41] Yamamoto Y, Baba N and Tajima S 1981 Coloured materials and photoluminescence centres in anodic film on aluminium *Nature* **289** 572–4
- [42] Gao T, Meng G and Zhang L 2003 Blue luminescence in porous anodic alumina films: the role of the oxalic impurities *J. Phys.: Condens. Matter* **15** 2071–9
- [43] Tajima S 1977 Luminescence, breakdown and colouring of anodic oxide films on aluminium *Electrochim. Acta* **22** 995–1011
- [44] Pashchanka M and Schneider J J 2011 Origin of self-organisation in porous anodic alumina films derived from analogy with Rayleigh–Bénard convection cells *J. Mater. Chem.* **21** 18761–7
- [45] Fukushima T, Fukuda Y, Ito G and Sato Y 1970 Anodic oxidation and local corrosion of aluminum in mono-carboxylic acids *J. Met. Finish. Soc. Japan* **21** 319–26
- [46] Noguchi H and Yoshimura C 1987 Effect of fluoride on anodization of aluminum in mono-carboxylic acid baths *J. Met. Finish. Soc. Japan* **38** 133–7
- [47] Bensalah W, Feki M, Wery M and Ayedi H F 2011 Chemical dissolution resistance of anodic oxide layers formed on aluminum *Trans. Nonferr. Met. Soc. China Eng. Ed.* **21** 1673–9
- [48] Moutarlier V, Gigandet M P, Pagetti J and Ricq L 2003 Molybdate/sulfuric acid anodising of 2024-aluminium alloy: influence of inhibitor concentration on film growth and on corrosion resistance *Surf. Coat. Technol.* **173** 87–95
- [49] Moutarlier V, Gigandet M P, Pagetti J and Normand B 2004 Influence of oxalic acid addition to chromic acid on the anodising of Al 2024 alloy *Surf. Coat. Technol.* **182** 117–23
- [50] Moutarlier V, Gigandet M P, Ricq L and Pagetti J 2001 Electrochemical characterisation of anodic oxidation films formed in presence of corrosion inhibitors *Appl. Surf. Sci.* **183** 1–9
- [51] García-Rubio M, Ocón P, Climent-Font A, Smith R W, Curioni M, Thompson G E, Skeldon P, Lavía A and García I 2009 Influence of molybdate species on the tartaric acid/sulphuric acid anodic films grown on AA2024 T3 aerospace alloy *Corros. Sci.* **51** 2034–42
- [52] Sieber M, Morgenstern R, Scharf I and Lampke T 2018 Effect of nitric and oxalic acid addition on hard anodizing of AlCu_4Mg_1 in sulphuric acid *Metals* **8** 1–15
- [53] Moutarlier V, Gigandet M P, Pagetti J and Linget S 2005 Influence of molybdate species added to sulphuric acid on composition and morphology of the anodic layers formed on 2024 aluminium alloy *Thin Solid Films* **483** 197–204
- [54] Klimas V, Naujokaitis A, Jankauskas S and Jagminas A 2022 Anodising of aluminium in formate solutions with formation of porous alumina arrays *Trans. IMF* **100** 333–41
- [55] Chernyakova K, Jasulaitiene V, Naujokaitis A, Karpicz R, Matulaitiene I, Klimas V and Jagminas A 2023 Aluminum anodizing in an aqueous solution of formic acid with ammonium heptamolybdate additive *J. Electrochem. Soc.* **170** 013501
- [56] Chernyakova K, Klimas V, Karpicz R, Naujokaitis A and Jagminas A 2023 Effect of oxalic acid additives on aluminum anodizing in formic acid containing ammonium heptamolybdate *J. Electrochem. Soc.* **170** 103511
- [57] Liu L, Li Y, Zhan L, Liu Y and Huang C 2011 One-step synthesis of fluorescent hydroxyls-coated carbon dots with hydrothermal reaction and its application to optical sensing of metal ions *Sci. China Chem.* **54** 1342–7
- [58] Daublytė E, Kalnaitytė M, Klimovich A, Drabavičius A and Charkova T 2023 Synthesis of silver nanoparticles with polyols under reflux and microwave irradiation conditions *Chemija* **34** 133–122
- [59] Yang S, Aoki Y, Skeldon P, Thompson G E and Habazaki H 2011 Growth of porous anodic alumina films in hot phosphate–glycerol electrolyte *J. Solid State Electrochem.* **15** 689–96
- [60] Sieber M, Morgenstern R and Lampke T 2016 Anodic oxidation of the AlCu_4Mg_1 aluminium alloy with dynamic current control *Surf. Coat. Technol.* **302** 515–22
- [61] Gabe D R and Gould S E 1988 Black molybdate conversion coatings *Surf. Coat. Technol.* **35** 79–91
- [62] Curioni M, Skeldon P, Koroleva E, Thompson G E and Ferguson J 2009 Role of tartaric acid on the anodizing and corrosion behavior of AA 2024 T3 aluminum alloy *J. Electrochem. Soc.* **156** C147
- [63] Samimi S, Maghsoudnia N, Eftekhari R B and Dorkoosh F 2019 Lipid-based nanoparticles for drug delivery systems *Characterization and Biology of Nanomaterials for Drug Delivery* (Elsevier) pp 47–76
- [64] Zheng C, Huang L, Guo Q, Chen W, Li W and Wang H 2018 Facile one-step fabrication of upconversion fluorescence carbon quantum dots anchored on graphene with enhanced nonlinear optical responses *RSC Adv.* **8** 10267–76
- [65] Wang Y and Hu A 2014 Carbon quantum dots: synthesis, properties and applications *J. Mater. Chem. C* **2** 6921
- [66] Dager A, Uchida T, Maekawa T and Tachibana M 2019 Synthesis and characterization of mono-disperse carbon quantum dots from Fennel seeds: photoluminescence analysis using machine learning *Sci. Rep.* **9** 14004
- [67] Devi S, Gupta R K, Paul A K and Tyagi S 2018 Waste carbon paper derivatized Carbon quantum dots/(3-aminopropyl)triethoxysilane based fluorescent probe for trinitrotoluene detection *Mater. Res. Express* **6** 025605
- [68] Ma X, Li S, Hessel V, Lin L, Meskers S and Gallucci F 2019 Chemical engineering and processing: process intensification synthesis of luminescent carbon quantum dots by microplasma process *Chem. Eng. Process.* **140** 29–35
- [69] Vrublevsky I A, Chernyakova K V, Ispas A, Bund A and Zavadski S 2014 Optical properties of thin anodic alumina membranes formed in a solution of tartaric acid *Thin Solid Films* **556** 230–5
- [70] Wang L et al 2014 Common origin of green luminescence in carbon nanodots and graphene quantum dots *ACS Nano* **8** 2541–7
- [71] Ding H, Yu S B, Wei J S and Xiong H M 2016 Full-color light-emitting carbon dots with a surface-state-controlled luminescence mechanism *ACS Nano* **10** 484–91
- [72] Li Z and Huang K 2007 The effect of high-temperature annealing on optical properties of porous anodic alumina formed in oxalic acid *Luminescence* **22** 355–61
- [73] Sun X, Xu F, Li Z and Zhang W 2006 Photoluminescence properties of anodic alumina membranes with ordered nanopore arrays *J. Lumin.* **121** 588–94
- [74] Zhu S, Song Y, Zhao X, Shao J, Zhang J and Yang B 2015 The photoluminescence mechanism in carbon dots (graphene quantum dots, carbon nanodots, and polymer dots): current state and future perspective *Nano Res.* **8** 355–81

- [75] Li J, Wang W, An B L, Jia X, Zhang Y H, Li J R, Bai Y L and Xu J Q 2022 Luminescence color regulation of carbon quantum dots by surface modification *J. Lumin.* **246** 118811
- [76] Mintz K J, Zhou Y and Leblanc R M 2019 Recent development of carbon quantum dots regarding their optical properties, photoluminescence mechanism, and core structure *Nanoscale* **11** 4634–52
- [77] Hesari M and Ding Z 2020 A perspective on application of carbon quantum dots in luminescence immunoassays *Front. Chem.* **8** 580033
- [78] Chernyakova K, Ispas A, Karpicz R, Ecke G, Vrublevsky I and Bund A 2020 Formation of ordered anodic alumina nanofibers during aluminum anodizing in oxalic acid at high voltage and electrical power *Surf. Coat. Technol.* **394** 125813
- [79] Shabbir H, Csapó E and Wojnicki M 2023 Carbon quantum dots: the role of surface functional groups and proposed mechanisms for metal ion sensing *Inorganics* **11** 262
- [80] Nguyen V, Si J, Yan L and Hou X 2016 Direct demonstration of photoluminescence originated from surface functional groups in carbon nanodots *Carbon* **108** 268–73
- [81] Rocco D, Moldoveanu V G, Feroci M, Bortolami M and Vetica F 2023 Electrochemical synthesis of carbon quantum dots *ChemElectroChem* **10** e202201104
- [82] Liu G, Zhao J, Wang S, Lu S, Sun J and Yang X 2020 Enzyme-induced in situ generation of polymer carbon dots for fluorescence immunoassay *Sens. Actuators B* **306** 127583
- [83] Alarfaj N A, El-Tohamy M F and Oraby H F 2020 New immunosensing-fluorescence detection of tumor marker Cytokeratin-19 fragment (CYFRA 21–1) via carbon quantum dots/zinc oxide nanocomposite *Nanoscale Res. Lett.* **15** 12